SAG: Stars and Galaxies **Vol. 8**, id. 3, 2025 December 0

Detection of weather variations on the exoplanet Qatar-1 b based on multi-wavelength transit observations

Yuya HIRANO[1] and Yoichi ITOH[1]
[1] *Center for Astronomy, University of Hyogo, 407-2 Nishigaichi, Sayo, Sayo, Hyogo 679-5313, Japan*
yitoh@nhao.jp

(Received 2025 October 31; accepted 2025 December 3)

Abstract

We conducted simultaneous transit observations of the exoplanet Qatar-1 b across multiple optical and near-infrared wavelengths from 2021 September 15 to 2023 October 12. The observations were carried out using the Nishi-Harima Infrared Camera (NIC) mounted on the Nayuta telescope and an optical imager on a 60 cm telescope at the Nishi-Harima Astronomical Observatory in Japan. We detected variations in radius ratios across these wavelengths and during the observational period, revealing three distinct patterns: small in the optical wavelengths and large in the near-infrared, large in the optical wavelengths and small in the near-infrared, and similar radius ratios at both wavelengths. These variations were not due to stellar spots but have been attributed to the presence of clouds or haze. Our observations indicated that Qatar-1b had a clear atmosphere on 2023 March 27, clouds or haze with a particle diameter of 0.1 μm or 0.01 μm on 2023 April 13, and clouds or haze with a particle diameter of 1.0 μm on 2023 October 12. Otherwise, the pressure at which clouds or haze exist varies between 1.0×10^{-5} bar and 8.0×10^{-4} bar. Observations at multiple wavelengths enable us to monitor temporal weather variations on exoplanets.

Key words: planets and satellites: gaseous planets — atmosphere — techniques: photometric

1. Introduction

We live on Earth, the third planet in the Solar System which exhibits a variety of natural features, including oceans, forests, deserts, and glaciers, with daily weather changes owing to atmospheric circulation. Weather phenomena primarily occur in the troposphere. Jupiter, the fifth planet, also has a troposphere with clouds composed of liquids particles, primarily NH_3 and H_2O (Atreya & Wong 2005). Neptune, the seventh planet, is suggested to have a troposphere with clouds of different compositions depending on altitude. The upper troposphere contains clouds from CH_4, whereas the lower troposphere has clouds composed of NH_3, H_2S, and H_2O (Elkins-Tanton 2006). Observations by the Huygens probe, part of the Cassini mission to Saturn, revealed that Saturn's moon, Titan, has a haze layer at an altitude of 500 km, composed of solid particles formed by complex photochemical reactions in Titan's atmosphere (Porco et al. 2005).

Various methods including the transit method, have been used to observe clouds and haze on exoplanets. The transit method involves detecting a decrease in stellar light when a planet passes in front of a star. If a planet has an atmosphere, specific wavelengths of light are absorbed by atmospheric molecules, allowing the composition of the planet's atmosphere to be estimated by analyzing the wavelength dependence of the radius ratios. However, if the planet is covered by clouds or haze, a flat spectrum without absorption features may be observed in the optical and near-infrared wavelengths.

Hot Jupiter, a type of giant gas planet that orbits very close to its star with an orbital period of only a few days, often have atmospheres composed primarily of H_2 and other molecules such as H_2O, CH_4, CO_2, and CO, which exhibit significant absorption in the near-infrared owing to their vibrational transitions. Intense ultraviolet radiation from the nearby star can trigger photochemical reactions, actively producing haze in the upper atmosphere.

Clouds on exoplanets were first observed on HD 189733b by Pont et al. (2013). The transmission spectrum of HD 189733b, obtained using the Hubble Space Telescope (HST) and Spitzer Space Telescope, exhibited no distinct spectral features at optical wavelengths (0.3 μm– 1 μm), except for a steep slope owing to Rayleigh scattering. In the infrared wavelengths (1 – 24 μm), no clear transmission spectrum features were found, suggesting that atmospheric absorption was masked by clouds or haze.

If clouds or haze in a planet's atmosphere change over time, the shape of the transmission spectrum is expected to change. We conducted simultaneous observations of exoplanet Qatar-1 b in optical and near-infrared wavelengths to investigate variations in radius ratios, attributing these variations to the presence of clouds or haze.

Qatar-1 is a star located approximately 190 pc from Earth in the Draco constellation. Alsubai et al. (2011) es-

timated the effective temperature of Qatar-1 to be 4861 ± 125 K using spectral data from the Tillinghast Reflector Echelle Spectrograph (TRES) on the 1.5 m Tillinghast reflector at the Fred Lawrence Whipple Observatory. The radius (R_*) was determined to be 0.823 ± 0.025 solar radii, with a mass of 0.85 ± 0.03 solar masses, a surface gravity of $\log g = 4.55 \pm 0.10$ cm s^{-2}, and a metallicity [Fe/H] of 0.20 ± 0.10 (Covino et al. 2013).

The exoplanet Qatar-1 b, discovered in 2011 using the Qatar Exoplanet Survey at the New Mexico Skies Observatory, has a radius of 1.164 ± 0.045 Jupiter radii, a mass of $1.090^{+0.084}_{-0.081}$ Jupiter masses, and an orbital period of 1.42 days, being classified as a hot Jupiter (Alsubai et al. 2011).

Despite long-term observations since its discovery, different studies reported different planetary radii at the same wavelength, which may be attributed to weather variations in the exoplanet's atmosphere. In optical R-band observations, Covino et al. (2013) reported the ratio of the planet radius to the stellar radius, R_p/R_*, to be 0.1513 ± 0.0008, while von Essen et al. (2017), Maciejewski et al. (2015), and Su et al. (2021) reported it to be 0.1435 ± 0.0008, $0.14591^{+0.00076}_{-0.00078}$, and $0.1456^{+0.0005}_{-0.0006}$, respectively. The differences in these radius ratios were larger than the measurement uncertainties.

In section 2, we describe the optical and near-infrared transit observations using a 2-meter Nayuta telescope and a 60 cm telescope. Section 3 describes the data-analysis procedures. Section 4 introduces the light curve fitting process. Section 5 presents the results, and section 6 discusses the variations in radius ratios.

2. Observations

Transit observations of Qatar-1 were conducted over 20 nights between 2021 September 15 and 2023 October 12. Observations utilized both the 2-meter Nayuta telescope and a 60 cm telescope at the Nishi-Harima Astronomical Observatory in Japan. The Nayuta telescope was equipped with a Nishi-Harima Infrared Camera (NIC) for near-infrared observations, while the 60 cm telescope employed the SBIG STL-1001E camera for optical observations. The NIC is equipped with three HgCdTe detectors, each with 1024×1024 pixels, enabling simultaneous observation in the near-infrared J-(1.25 μm), H-(1.63 μm), and Ks-(2.15 μm) bands. The STL-1001E has a 1024×1024 pixels CCD sensor. During the observations of Qatar-1, the Johnson V-band was used.

The field of view of NIC is $2'.73 \times 2'.73$, whereas the STL-1001E has a field of view of $11'.6 \times 11'.6$. A 10-position dithering pattern with a radius of 10 $''$ was applied during NIC observations to mitigate the impact of bad pixels, which are more prevalent in near-infrared detectors compared to optical CCDs. Observations were scheduled according to the predicted transit times provided by the TESS Transit Finder (Jensen 2013). Observations began 1 h before the start of transit and continued until 1 h after transit ended, resulting in a total observation duration of approximately 4 h. Depending on weather conditions, pre- and post-transit observation periods were sometimes extended. The exposure times were set to 60 s for NIC and 30 s for STL-1001E. Dark and dome-flat frames were obtained after observations. For flat-field correction of images acquired with NIC, a previously obtained master twilight flat frame was used.

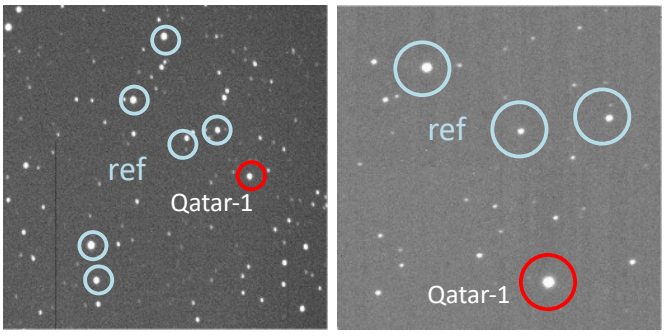

Fig. 1. Examples of the optical V-band image (left) and the near-infrared H-band image of Qatar-1. Qatar-1 and the reference stars are marked by red and light-blue circles, respectively. North is up and east to left for both images.

3. Data reduction

Data reduction was performed using the Image Reduction and Analysis Facility (IRAF) software. Initial steps included dark subtraction, flat fielding, and correction of bad pixels. For images obtained with NIC, sky subtraction was performed to correct for OH airglow and thermal emission. A sky pattern was created by combining ten dithered images using the median, which was then subtracted from the data. After sky subtraction, a vertical stripe pattern, unique to NIC and caused by voltage variations during detector readout column switching, remained. Due of the varying vertical stripe patterns in each image, we extracted and removed the vertical stripes from areas without stars. The pixel values affected by cosmic rays were corrected by interpolating the values of surrounding pixels. Examples of the near-infrared image as well as the optical image are shown in figure 1.

Photometry was conducted using aperture photometry. The relative flux was calculated by dividing the flux of the target star by the sum of the fluxes of photometric reference stars. To improve photometric accuracy, multiple reference stars were used, selected based on the following criteria: they are within $10'$ of Qatar-1, and they had counts e^- of at least 100,000 during the observation period. The brightness of reference stars was verified to be stable by comparing the flux of one reference star to another. The reference stars used in this study are listed in table 1.

Photometry was performed using aperture radii of 1.0, 1.5, and 2.0 times the full width at half maximum (FWHM) of the point spread function (PSF), which varied for each image. An aperture radius of 1.5 times the FWHM of the PSF was chosen to achieve the smallest standard deviation of relative flux outside the transit, with radii ranging from $1''.5$ to $4''.0$. Subsequently, a regres-

Table 1. Photometric reference stars

Star ID	RA (J2000)	Dec (J2000)	V Mag	NIC	60 cm
TYC 4240-1343-1	20h 13m 57s	+65°15 ′08 ″	12.0	No	Yes
TYC 4240-905-1	20h 14m 10s	+65°12 ′55 ″	11.7	No	Yes
TYC 4240-34-1	20h 14m 29s	+65°07 ′45 ″	11.1	No	Yes
2MASS J20142800+6506270	20h 14m 28s	+65°06 ′27 ″	...	No	Yes
USNO-B1.0 1551-0215477	20h 13m 41s	+65°11 ′33 ″	...	No	Yes
USNO-B1.0 1551-0215437	20h 13m 52s	+65°11 ′21 ″	...	Yes	Yes
USNO-B1.0 1551-0215401	20h 13m 34s	+65°11 ′02 ″	...	Yes	No
USNO-B1.0 1551-0215373	20h 13m 27s	+65°11 ′08 ″	...	Yes	No

sion line was obtained using the relative flux outside the transit, and these values were normalized to 1. In addition, there was a positional dependence of the relative flux due to dithering observations with NIC, potentially arising from imperfections in the flat-field correction as noted by Tabata & Itoh (2020). The average relative flux outside of the transit was derived for each dithering position, and the relative flux of the corresponding images at the same position was divided by the average to eliminate the position dependence. Finally, the standard deviation of the relative flux was calculated for pre-transit, in-transit, and post-transit intervals from the expected transit time, with outliers beyond 2σ removed.

4. Light curve fitting

We used the transit modeling tool, BAsic Transit Model cAlculatioN (batman) (Kreidberg 2015), to perform transit model fitting and determine the planet-to-star radius ratio. The input data consisted of the observed times, the relative flux, and the standard deviation of the relative flux obtained with the transit observations. The transit center time, orbital period, semi-major axis, orbital inclination, eccentricity, and argument of periastron were fixed as the model parameters. The parameters to be determined are the radius ratio, the order of the baseline fit, and the limb darkening model. The analysis began by varying the planet-to-star radius ratio between 0.08 and 0.18 in 0.01 increments. We used linear and quadratic functions for baseline fitting. For the limb darkening model, we evaluated the linear, quadratic, square-root, and logarithmic models. The coefficients were obtained from Claret, Hauschildt, & Witte (2012) and set according to each observational band (table 2). Degree of the fitting was evaluated with the Bayesian Information Criterion (BIC). BIC was calculated based on the residuals between the relative flux and the model (Raftery 1995). BIC is defined as

$$BIC = \chi^2 + k\ln(n), \tag{1}$$

where χ^2 is a measure of the deviation between the observed data and the model predictions, defined by the following equation:

$$\chi^2 = \sum_{i=1}^{n} \frac{(f_{i,\mathrm{obs}} - f_{i,\mathrm{model}})^2}{\sigma_i^2}, \tag{2}$$

where $f_{i,\mathrm{obs}}$ is the observed flux at time i, $f_{i,\mathrm{model}}$ is the model flux, and σ_i is the standard deviation of the observed relative flux. A smaller χ^2 indicates a better fit of the model to the data. k is the degree of freedom, and n is the number of data points. The model with the lowest BIC is considered the best fit. The optimal model was determined by selecting the combination of the baseline fitting and the limb darkening models with the lowest BIC, providing an initial estimate of the planet-to-star radius ratio. BIC values ranged from 62.7 to 820.5 (table 3). The linear baseline combined with the linear limb darkening model was identified as the best fit for all transits.

Next, we evaluated the red noise. In ground-based photometry, time-correlated noise (red noise) exists, which is caused by temporal variations in the transparency of the Earth's atmosphere. The red noise was evaluated using the time-averaging method (Winn et al. 2007) for each transit light curve. First, the residuals between the relative flux and the model were calculated, and the standard deviation of all the data, σ_A, was derived. Then, the data were binned into M bins, with each bin containing 10 frames. For each bin, we calculated the standard deviation of the residuals, denoted as $\sigma_{N,obs}$. The standard deviation of the data without red noise, $\sigma_{N,calc}$, was calculated according to the following equation,

$$\sigma_{N,calc} = \frac{\sigma_A}{\sqrt{10}} \times \sqrt{\frac{M}{M-1}}. \tag{3}$$

The term $\sqrt{M/M-1}$ is a statistical correction factor (Winn et al. 2008). This correction is necessary when the number of bins is small. As M increases, this term approaches 1. In our observations, M ranged from 8 to 38. If the noise is purely random with no time correlation, the standard deviation decreases inversely with the square root of the number of data points in each bin. However, in real observations, red noise is often present, causing $\sigma_{N,obs}$ to be larger than $\sigma_{N,calc}$. To correct for this difference, we used the beta factor to adjust for the actual noise level. The beta factor, β, was calculated as

$$\beta = \frac{\sigma_{N,obs}}{\sigma_{N,calc}}. \tag{4}$$

The median of the beta factors across all bins was used as the final β. When the final β was less than 1, it was fixed to 1 to avoid underestimating the red noise correction. The β values ranged from 1.00 to 3.11 (table 3). The observed relative flux standard deviation was multiplied by β, and the adjusted standard deviation was subsequently

Table 2. Limb darkening coefficients for each observational band (Claret, Hauschildt, & Witte 2012)

Band	Linear (u)	Quadratic (a, b)	Square-root (c, d)	Logarithmic (e, f)
V	0.7698	0.7300, 0.0591	0.6577, 0.1726	0.8028, 0.0634
J	0.4269	0.2872, 0.2077	0.0295, 0.6116	0.5435, 0.2242
H	0.3535	0.1462, 0.3082	-0.2416, 0.9160	0.5276, 0.3347
Ks	0.2967	0.1307, 0.2467	-0.1806, 0.7345	0.4362, 0.2682

applied to refit the data.

The final planet-to-star radius ratio and its uncertainty, accounting for red noise, were obtained using a Markov Chain Monte Carlo (MCMC) method. The initial parameter was set to the previously determined radius ratio. The MCMC analysis was conducted with 50 walkers and 10,000 steps per walker, utilizing the optimal model identified in the prior analysis, which consisted of the linear baseline fit and the linear limb darkening model. Once the variation in the radius ratio output from 10,000 steps converged to within 1%, we considered the radius ratio to be determined. The planet-to-star radius ratio and its uncertainty were thus obtained for each transit.

5. Results

We observed Qatar-1's transit events over seven nights in the V-band, three nights in the J-, H-, and Ks-bands, and ten nights in the V-, J-, H-, and Ks-bands. Of the 20 nights of observation, the transit was successfully detected on seven nights. The observed radius ratios varied between 0.122 and 0.161 in the V-band, between 0.107 and 0.148 in the J-band, between 0.125 and 0.143 in the H-band, and between 0.092 and 0.142 in the Ks-band (table 3). The radius ratios exhibited variation across different wavelengths and revealed three distinct patterns (figure 2):

1. A smaller radius ratio in optical wavelengths and a larger radius ratios in near-infrared wavelengths (2023 March 27).
2. A larger radius ratio in optical wavelengths and smaller radius ratios in near-infrared wavelengths (2023 April 13).
3. Similar radius ratios in both optical and near-infrared wavelengths (2023 October 12).

Notably, the radius ratios in the V-band varied by approximately 30% between 2023 March 27 and 2023 April 13.

6. Discussion

Observations conducted between 2021 September 15 and 2023 October 12 revealed variations in radius ratios across multiple wavelengths. We focused on three specific patterns observed on 2023 March 27, 2023 April 13 and 2023 October 12. Two phenomena were considered to be the cause of the observed variations in radius ratios: stellar variability due to starspot activity, and atmospheric variability of the planet.

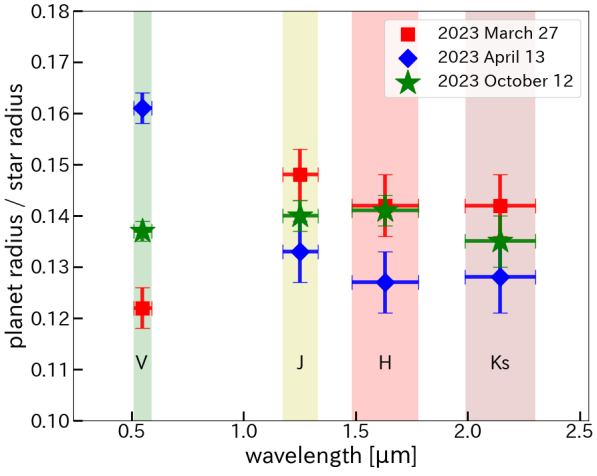

Fig. 2. The planet-to-star radius ratios for the V, J, H, and Ks bands. Symbols represent observations on specific dates: 2023 March 27 (red squares), 2023 April 13 (blue diamonds), and 2023 October 12 (green stars). The shaded regions indicate wavelength bands V, J, H, and Ks. The vertical bars represent uncertainties in the measurements. The observed patterns are as follows: a small radius ratio in optical wavelengths and a larger radius ratio in near-infrared wavelengths (2023 March 27), a larger radius ratio in optical wavelengths and a smaller radius ratio in near-infrared wavelengths (2023 April 13) and similar radius ratios in both optical and near-infrared wavelengths (2023 October 12).

6.1. Star spots

First, we examined starspots on the host star as a potential cause of variations in radius ratios. Starspots are cooler than the photosphere, leading to a decrease in overall flux from the star and an increase in radius ratios. The effective temperature of Qatar-1 is 4800 K, while the temperature of the starspots is estimated to be 3600 K based on the empirical formula proposed by Notsu et al. (2019). The observed radius ratio is expressed as (Parviainen et al. 2016):

$$\frac{\Delta F}{F} = \left(\frac{R_{\rm p}}{R_*}\right)^2 \left(\frac{1}{1-fA}\right), \tag{5}$$

where

$$A = 1 - \frac{P(\lambda,\ 3600K)}{P(\lambda,\ 4800K)}. \tag{6}$$

where $R_{\rm p}$ is the radius of the planet, R_* is the radius of the host star, f is the spot-filling factor, A is the wavelength-dependent contrast ratio, and P denotes Planck's function. Assuming no starspots ($f = 0$) during the transit

Table 3. Observed radius ratios of Qatar-1 b in various bands

Date	Obs-Time (UTC)	Band	BIC	β	R_p/R_s
2021 September 15	14:13-18:26	J	180.3	1.00	0.107 ± 0.007
		H	87.7	1.16	0.129 ± 0.006
		Ks	404.4	1.15	0.137 ± 0.005
2022 July 6	13:00-17:05	J	155.9	1.00	0.136 ± 0.007
		H	76.0	1.08	0.137 ± 0.007
		Ks	268.4	1.09	0.132 ± 0.007
2022 October 29	13:53-17:25	J	287.0	1.29	0.144 ± 0.006
		H	171.4	1.07	0.125 ± 0.008
		Ks	121.4	1.00	0.092 ± 0.011
2023 March 27	15:28-19:49	V	159.1	1.46	0.122 ± 0.004
	15:53-20:05	J	136.8	1.10	0.148 ± 0.005
		H	89.0	1.00	0.142 ± 0.006
		Ks	245.0	1.03	0.142 ± 0.006
2023 April 13	15:45-20:07	V	820.5	1.68	0.161 ± 0.003
	16:22-20:21	J	128.4	1.10	0.133 ± 0.006
		H	143.6	2.61	0.127 ± 0.006
		Ks	273.8	1.00	0.128 ± 0.007
2023 May 10	16:32-19:39	J	86.62	3.11	0.136 ± 0.006
		H	62.7	1.00	0.143 ± 0.005
		Ks	263.6	1.17	0.140 ± 0.005
2023 October 12	11:14-15:38	V	372.1	1.56	0.136 ± 0.002
	10:58-15:11	J	187.2	1.21	0.140 ± 0.003
		H	139.7	1.23	0.141 ± 0.003
		Ks	140.6	1.33	0.135 ± 0.005

on March 27, we estimate that to explain the 32% increase in radius ratio observed in the V-band on April 13, starspots must cover 29% of the stellar surface. In this case, the radius ratios would increase by 20% in the J-band, 17% in the H-band, and 15% in the Ks-band on April 13. However, observations on April 13 showed that the radius ratios showed a decrease in the J-, H-, and Ks-bands. Therefore, variations in radius ratios are unlikely to be attributed to starspots.

6.2. Clear atmosphere

Next, we consider the variations caused by clouds or haze particles in the atmosphere. We created a model spectrum of the planetary atmosphere using the Planetary Spectrum Generator (PSG) (Villanueva et al. 2018), an online radiative transfer code that generates model spectra of planetary atmospheres. The vertical temperature profile of the planet was determined using the non-grey analytical model developed by Parmentier & Guillot (2014), which simplifies the numerical solution of radiative transfer equations originally derived by Fortney et al. (2008). PSG selects atmospheric molecular species and aerosol types. Necessary parameters for creating atmospheric model spectra such as the planet's diameter, surface gravity, semi-major axis, host star spectral type, and temperature were obtained from NASA's Exoplanet Archive.

We first created atmospheric model spectra for a planet with a clear atmosphere. As Qatar-1 b is a hot Jupiter, we assumed that the planet's atmosphere is composed of H_2 with a volume abundance of 99%. The remaining 1% was set as a single molecule such as CH_4 or NH_3 (e.g., 99% H_2, 1% H_2O). To match the observational results, the planet's diameter was varied from 0.5 to 1.5 times the original 163,000 km (in increments of 0.1). At wavelengths where the molecular constituents absorb strongly, the atmosphere can be opaque over several scale heights (Deming, Louie, & Sheets 2018). Yelle (2004) and Koskinen et al. (2013) demonstrated that stellar XUV radiation can heat the thermosphere of hot Jupiters. In addition to this radiative heating, turbulence may enhance the vertical mixing of molecules, further affecting the atmospheric expansion. As a result, the planet's upper atmosphere results in a larger effective scale height. To account for this inflation, we introduced an expansion factor into our atmospheric model. Expanded atmosphere results in stronger molecular absorption in the upper layers, leading to larger observed radius ratios in the near-infrared. This scaling factor modifies b_s the scale height according to the equation,

$$H' = \frac{kT}{\mu g} \times b_s. \tag{7}$$

Here, k represents the Boltzmann constant, T is the atmospheric temperature, μ is the mean molecular weight, and g is the surface gravity of the planet. The parameter b_s was adjusted from 10^{-2} to 10^2 in logarithmic steps of 1.0. If 10^0 was deemed suitable, it was further adjusted in increments of 10^0 up to 9×10^0 as required. This adjustment was based on the expanded scale height equation to model the effects of atmospheric inflation more accurately. Multiple planetary atmospheric model spectra were cre-

ated by exponentially varying the pressure. The pressure was adjusted from 10^1 to 10^{-6} bar in logarithmic steps of 1.0. If 1.0×10^{-2} bar was deemed suitable, it was adjusted in 1.0×10^{-2} increments up to 9.0×10^{-2} as required. This pressure corresponds to the altitude where τ reaches 1 at optical wavelengths. The radius ratios of the model spectra were calculated by multiplying the atmospheric model spectra to the filter transmittance for the V-, J-, H-, and Ks-bands. We found that a spectral model with 99% H_2 and 1% NH_3, a mean molecular weight of 2.15 g/mol, a planetary diameter of 114,100 km (0.7 times the original), a scaling factor b_s of 10, and a pressure of 5.0×10^{-1} bar minimized the difference between the model and the observational radius ratios observed on 2023 March 27 (figure 3). In the atmosphere of hot Jupiters like Qatar-1b, where temperatures exceed 1000K, it is thought that large quantities of NH_3 are unlikely to exist due to thermochemical reactions. MacDonald & Madhusudhan (2017) observed absorption features of NH_3 that were 10^4 times stronger than expected by chemical equilibrium, suggesting that this high NH_3 abundance could be due to vertical mixing, which transports material from the deeper atmosphere to the upper layers. This mechanism includes the transport of NH_3 from the deeper, more stable regions of the atmosphere to the upper layers, where photodissociation may occur at higher altitudes. If vertical mixing is sufficiently strong, it can supply enough NH_3 to the upper atmosphere to account for the observed absorption features.

We assumed the presence of vertical mixing to explain the observed features and used an atmospheric model that includes 1% NH_3 in the upper atmosphere.

It is unlikely for NH_3 to exist in such high abundance, but the 1% value was used as a simplification for examining key absorption features. This setting is effective in the early stages of atmospheric studies with limited data such as ground-based observations. This model spectrum reproduced the smaller observed radius ratio in the optical V-band and larger radius ratios observed in the near-infrared J-, H-, and Ks-bands. However, the larger radius ratio in the optical V-band and smaller radius ratios in the near-infrared J-, H-, and Ks-bands observed on 2023 April 13 were not explained by a clear atmosphere. Observations on October 12 revealed that the radius ratio in the optical and near-infrared wavelengths remained almost constant across these wavelengths. Identifying the specific molecules present in the atmosphere proved challenging.

6.3. Cloudy or hazy atmosphere

Next, we consider the atmospheric model spectra where the planet contains clouds. If cloud formation and dissipation cause variations in the radius ratios of Qatar-1 b, it is likely that the easily condensible atmospheric molecules, like NH_3, form clouds rather than H_2. To investigate the temperature structure of a planet's atmosphere, we constructed a P-T diagram for Qatar-1 b based on a nongray analytical model from Parmentier & Guillot (2014). The temperature at 1 bar was approxi-

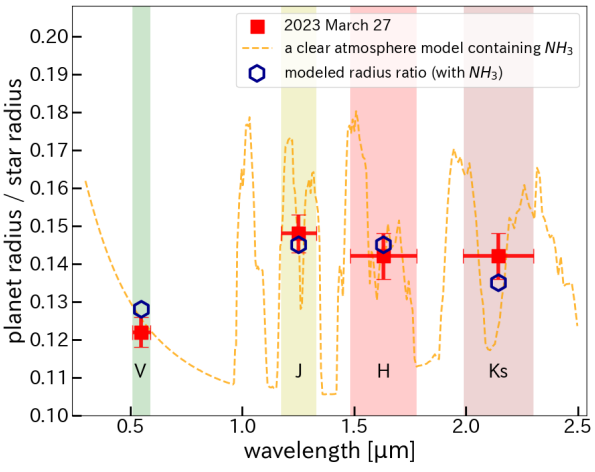

Fig. 3. Observed planet-to-star radius ratios of Qatar-1 b on March 27 compared to the clear atmospheric model spectrum. The red squares indicate the radius ratios observed on 2023 March 27. The orange dashed line represents a clear atmospheric model spectrum with H_2 99%, NH_3 1%, a mean molecular weight of 2.15 g/mol, planetary diameter of 114,100 km (0.7 times the original), an expansion factor b_s of 10, and pressure of 5.0×10^{-1} bar. The dark blue hexagons show the radius ratios of the atmospheric model corrected for the filter transmittance in each band.

mately 1600 K and gradually decreased to approximately 1100 K at 10^{-2} bar. Above 10^{-2} bar, the temperature remained nearly constant at 1100 K. As the condensation temperature of NH3 is less than 200 K, NH_3 clouds do not exist. Instead, high-temperature clouds such as those composed of TiO_2 or Fe may be present. These atoms and molecules do not exhibit prominent absorption features for the near-infrared J-, H-, and Ks-bands. We used the Simple-GSFC cloud model (Bohren & Huffman 1983) to simulate these conditions. For the input parameters, we fixed the atmospheric composition to 99% H_2 and 1% NH_3, a mean molecular weight of 2.15 g/mol, with a planetary diameter of 114,100 km and an expansion factor b_sb of 10. The pressure varied from 10^0 to 10^{-6} bar, similar to those of the clear atmospheric model. This corresponds to the altitude where τ reaches 1 at optical wavelengths. We varied the cloud particle diameters (1, 0.1, 0.01 μm) and the mass abundance of clouds relative to the entire atmosphere (1%, 0.1%, 0.01%, 0.001%) to generate different model spectra. A cloud model spectrum with these parameters, a cloud particle diameter of 0.1 μm, a cloud mass abundance of 0.1%, and a pressure of 4.0×10^{-4} bar was consistent with the observational radius ratios on April 13, showing a larger radius ratio in the optical V-band and smaller radius ratios in the near-infrared J-, H-, and Ks-bands (figure 4). Similar radius ratios across optical and near-infrared wavelengths observed on October 12 were reproduced using another cloud model with a particle diameter of 1 μm, cloud mass abundance of 1%, and pressure of 1.0×10^{-5} bar (figure 5). In this model, the pressure in the region where τ equals 1 is 4.0×10^{-4} bar

on April 13 and 1.0×10^{-5} bar on October 12. Within this range, the temperature remained nearly constant at 1100 K, supporting the presence of clouds like KCl, ZnS, Na_2S, MnS, and Cr, which could produce nearly constant radius ratios from optical to near-infrared wavelengths due to Mie scattering, matching the observational results.

Next, we considered haze. If the planet has an NH_3 atmosphere, then N_2 molecules are expected to remain in the atmosphere. Titan has a nitrogen-dominated atmosphere and is covered by haze. Thus, it is possible that the haze in Qatar-1 b's atmosphere has a composition similar to the haze of Titan. Estrela, Swain, & Roudier (2022) found that exoplanet hazes are much more widespread than those on Jupiter, peaking at approximately 10^{-2} bar but the densities remain nearly constant up to 10^{-6} bar. We used the Khare-Titan-Tholin-HRI model (Khare et al. 1984) with input parameters varied similarly to those in the cloud model to generate different model spectra. Haze, like clouds, is concentrated in the lower atmosphere with decreasing density in the upper layer. By using a haze model consisting of 99% H_2 and 1% NH_3, a mean molecular weight of 2.15 g/mol, the planetary diameter of 114,100 km, an expansion factor b_s of 10, the haze-particle diameter of 0.01 μm, the mass abundance of haze relative to the entire atmosphere of 1%, and pressure of 8.0×10^{-4} bar, this model spectrum reproduced a larger radius ratio in the optical V-band and smaller radius ratios in the near-infrared J-, H-, and Ks-bands observed on April 13 (figure 4). Another haze model with a haze particle diameter of 1 μm, the mass abundance of haze relative to the entire atmosphere of 1%, and pressure of 2.0×10^{-5} bar supported the observations from October 12, showing similar radius ratios at both optical and near-infrared wavelengths (figure 5). In haze models with smaller particle diameters, Rayleigh scattering causes larger radius ratios at optical wavelengths and smaller radius ratios at near-infrared wavelengths. In models with larger particle diameters, Mie scattering results in nearly constant radius ratios across these wavelengths.

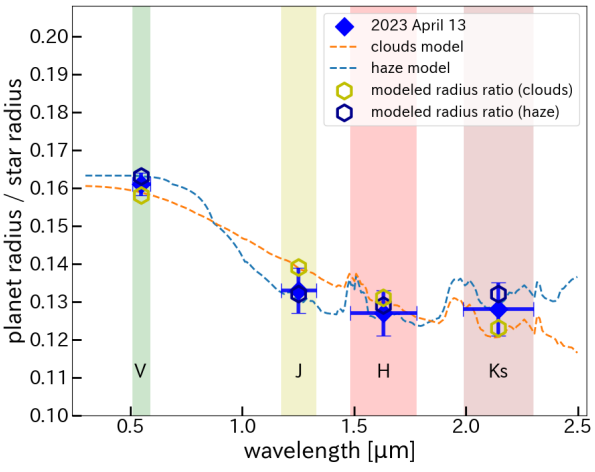

Fig. 4. Observed planet-to-star radius ratios of Qatar-1 b on April 13 compared to cloud and haze model spectra. The blue diamonds represent the radius ratios observed on 2023 April 13. The orange dashed line represents a cloud model spectrum with H_2 99%, NH_3 1%, a mean molecular weight of 2.15 g/mol, planetary diameter of 114,100 km (0.7 times the original), an expansion factor b_s of 10, the cloud particle diameter of 0.1 μm, the mass abundance of clouds relative to the entire atmosphere of 0.1%, and the pressure of 4.0×10^{-4} bar. The blue dashed line represents a haze model spectrum with H_2 99%, NH_3 1%, a mean molecular weight of 2.15 g/mol, planetary diameter of 130,400 km (0.8 times the original), an expansion factor b_s of 10, the haze particle diameter of 0.01 μm, the mass abundance of haze relative to the entire atmosphere of 1%, and the pressure of 8.0×10^{-4} bar. The yellow and dark blue hexagons show the radius ratios of the atmospheric model corrected for the filter transmittance in each band.

6.4. *Formation and dissipation process of clouds and haze*

Spectral variations due to dust formation and dissipation have been observed in brown dwarfs (Stephens et al. 2009). In these objects, dust forms as the temperature decreases at high altitudes, causing gas supersaturation and facilitating dust nucleation and growth. The formed dust settles, eventually evaporating as it approaches warmer atmospheric layers. Woitke & Helling (2003) estimated that the gravitational settling timescale of dust in brown dwarfs was approximately 15 min for particles with a diameter of 100 μm, but approximately eight months for particles with diameters of 0.1 μm.

The weather on Qatar-1 b is summarized in table 4. The rapid formation and dissipation of clouds and haze likely account for the observed variations in the radius ratios. On March 27, the atmosphere was believed to be clear, resulting in a small radius ratio at optical wavelengths and a large radius ratio at near-infrared wavelengths. However, clouds or haze present on April 13 caused a large radius ratio in the optical wavelengths and a small radius ratio at near-infrared wavelengths. Distinguishing between clouds and haze is challenging since no distinct absorption features were observed from the V-band (0.55 μm) to the Ks-band (2.15 μm). The short time span between observations on March 27 and April 13 suggests an efficient process of cloud and haze formation and dissipation, possibly occurring within weeks. Theoretically, the dust formation is predicted to be complete within a few seconds (Helling, Klein, & Sedlmayr 2005).

Particle diameter may have changed from April 13 to October 12 due to particle growth. Thus, it was inferred that the atmosphere was clear on March 27, cloudy with particle diameters of 0.1 μm or 0.01 μm on April 13. and cloudy, with a particle diameter of 1.0 μm on October 12. Otherwise, it is suggested that the pressure where clouds exist changes from 1.0×10^{-5} bar to 8.0×10^{-4} bar between April 13 and October 12. This pressure correlates with the altitude where clouds are present. Higher pressures correspond to lower altitudes, while lower pressures correspond to higher altitudes.

Mannaday et al. (2022) analyzed 98 transit light curves of Qatar-1 b observed by the Transiting Exoplanet Survey

Table 4. Summary of models used to reproduce the planet-to-star radius ratios observed in this study

Date	Model	Pressure (bar)	Diameter (μm)	Abundance (%)
2023 March 27	clear	5.0×10^{-1}	-	-
2023 April 13	cloud	4.0×10^{-4}	0.1	0.1
	haze	8.0×10^{-4}	0.01	1
2023 October 12	cloud	1.0×10^{-5}	1	1
	haze	2.0×10^{-5}	1	1

Satellite (TESS). These data were primarily used to investigate transit timing variations. The planet-to-star radius ratio for each transit was also compiled into a database. Using this database, we compared the radius ratios of Qatar-1 b. The observational wavelength range of TESS is 0.6-1.0 μm. The radius ratio of Qatar-1 b ranged from 0.1341 to 0.1636, showing a maximum variation of 22%. The radius ratio on 2020 May 18 was $0.1636^{+0.0098}_{-0.009}$, while it was $0.1363^{+0.0042}_{-0.0041}$ on 2020 June 1, indicating a 20% change over two weeks. This variation occurred on the same timescale as the 30% change observed in this study between 2023 March 27 and 2023 April 13. These findings suggest that the formation and dissipation of clouds in the planetary atmosphere occur on short timescales. Furthermore, if radius variations of several tens of percent observed by space telescopes can also be revealed from the ground, the significance of ground-based observations would be greatly enhanced. In particular, multi-wavelength observations using multiple telescopes could complement space telescope data and allow the detection of weather variations in planetary atmospheres.

7. Conclusions

We conducted simultaneous transit observations of exoplanet Qatar-1 b at multiple wavelengths in the optical and near-infrared wavelengths from 2021 September 15 to 2023 October 12. Our results indicated that time variations in the radius ratios were observed across these wavelengths. These variations were not due to stellar spots or changes in the transit path but were caused by the presence or absence of clouds or haze, by particle growth, or altitude change of cloud or haze. Observing transits at multiple wavelengths facilitates monitoring temporal weather variations in exoplanets.

Acknowledgments

This work was supported by JST SPRING, Japan Grant Number JPMJSP2175. We would like to thank Editage (www.editage.jp) for English language editing. We thank to Dr. Jun Takahashi, Dr. Miyako Tozuka, Dr. Masaki Takayama, Dr. Tomoki Saito, and Dr. Jun Toshikawa for telescope operation.

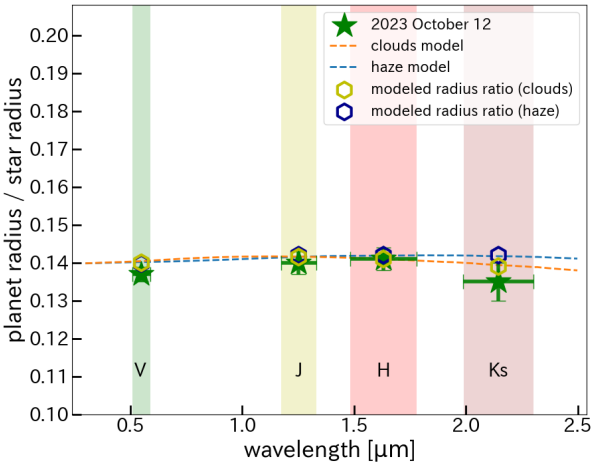

Fig. 5. Observed planet-to-star radius ratios of Qatar-1 b on October 12 compared to cloud and haze model spectra. The green stars represent the radius ratios observed on 2023 October 12. The orange dashed line represents a cloud model spectrum with H_2 99%, NH_3 1%, a mean molecular weight of 2.15 g/mol, planetary diameter of 114,100 km (0.7 times the original), an expansion factor b_s of 10, the cloud particle diameter of 1.0 μm, the mass abundance of clouds relative to the entire atmosphere of 1%, and the pressure of 1.0×10^{-5} bar. The blue dashed line represents a haze model spectrum with H_2 99%, NH_3 1%, a mean molecular weight of 2.15 g/mol, planetary diameter of 130,400 km (0.8 times the original), an expansion factor b_s of 10, the haze particle diameter of 1.0 μm, the mass abundance of haze relative to the entire atmosphere of 1%, and the pressure of 2.0×10^{-5} bar. The yellow and dark blue hexagons show the radius ratios of the atmospheric mode l corrected for the filter transmittance in each band.

Appendix 1. Qatar-1 b transit light curves in various bands

This appendix presents the transit light curves of Qatar-1 b observed across multiple dates from 2021 to 2023 in the V, J, H, and Ks bands. The observed relative flux data are plotted alongside the model fluxes, with residuals (O-C) (figure 6, figure 7).

Appendix 2. Validation of the 2023 April 13 V-band observation

The V-band post-transit observation on 2023 April 13 was limited to 20 minutes due to twilight. To validate the reliability of the derived radius ratio from the 2023 April

13 observations, we utilized the V-band observations from 2023 October 12, which included a sufficient post-transit baseline. The standard deviation of the residuals in the April 13 observation was 0.011 in the pre-transit, 0.015 in the in-transit, and 0.027 in the post-transit. In comparison, the October 12 observation had a standard deviation of 0.007 in the pre-transit, 0.007 in the in-transit, and 0.010 in the post-transit. To simulate the conditions of the 2023 April 13 observation, we artificially degraded the data quality of the 2023 October 12 dataset by multiplying the residuals by factors of 1.57, 2.14, and 2.70 in the pre-transit, in-transit, and post-transit, respectively. Subsequently, the adjusted residuals were added to the model fit curve to reproduce the observed data for April 13. As a result, the standard deviations increased to 0.011 in the pre-transit, 0.015 in the in-transit, and 0.027 in the post-transit.

Additionally, we systematically shortened the post-transit baseline in increments of 10 minutes, starting from the end of the observation. For each truncated dataset, light curve fitting was performed, and the quality of the fit was evaluated using the Bayesian Information Criterion (BIC). The model with the smallest BIC value was selected as the best fit for each data set. The baseline models tested included both linear and quadratic functions, while the limb darkening models considered were linear, quadratic, square root, and logarithmic. Across all datasets, the best-fitting model consisted of a linear baseline and a linear limb darkening model.

The analysis showed that the radius ratio remained stable at 0.137, even when the post-transit baseline was entirely removed. Variations in the radius ratio appeared when the transit segment itself was shortened by 10 minutes, resulting in a radius ratio of 0.140. These results demonstrate that the radius ratio derived from the 2023 April 13 observation is robust and not significantly influenced by the limited post-transit baseline. Figure 8 summarizes the light curves and residuals for each dataset, showing the stability of the radius ratio under different baseline conditions.

References

Alsubai, K. A., et al. 2011, MNRAS, 417, 709
Atreya, S. K., & Wong, A. S. 2005, Space Sci. Rev., 116, 121
Bohren, C. F., & Huffman, D. R. 1983, Absorption and Scattering of Light by Small Particles (New York: Wiley)
Claret, A., Hauschildt, P. H., & Witte, S. 2012, A&A, 546, A14
Covino, E., et al. 2013, A&A, 554, A28
Deming, D., Louie, D., & Sheets, H. 2018, PASP, 131, 013001
Elkins-Tanton, L. T. 2006, Uranus, Neptune, Pluto, and the Outer Solar System (New York: Chelsea House), ch. 7
Estrela, R., Swain, M. R., & Roudier, G. M. 2022, ApJL, 941, L5
Fortney, J. J., Lodders, K., Marley, M. S., & Freedman, R. S. 2008, ApJ, 678, 1419
Helling, C., Klein, R., & Sedlmayr, E. 2005, The Multi-scale Dust Formation in Substellar Atmospheres (Berlin: Springer Berlin Heidelberg)
Heng, K., & Kitzmann, D. 2017, MNRAS, 470, 2972
Jensen, E. 2013, Astrophysics Source Code Library, ascl:1306.007
Khare, B. N., Sagan, C., Arakawa, E. T., Suits, F., Callcott, T. A., & Williams, M. W. 1984, Icarus, 60, 127
Koskinen, T. T., Harris, M. J., Yelle, R. V., & Lavvas, P. 2013, Icarus, 226, 1678
Kreidberg, L. 2015, PASP, 127, 1161
MacDonald, R. J., & Madhusudhan, N. 2017, ApJL, 850, L15
Maciejewski, G., et al. 2015, A&A, 577, A109
Mannaday, V. K., et al. 2022, AJ, 164, 198
Notsu, Y., et al. 2019, ApJ, 876, 58
Parmentier, V., & Guillot, T. 2014, A&A, 562, A133
Parviainen, H., Pallé, E., Nortmann, L., Nowak, G., Iro, N., Murgas, F., & Aigrain, S. 2016, A&A, 585, A114
Poddaný, S., Brát, L., & Pejcha, O. 2010, New Astron., 15, 297
Pont, F., Sing, D. K., Gibson, N. P., Aigrain, S., Henry, G., & Husnoo, N. 2013, MNRAS, 432, 2917
Porco, C. C., et al. 2005, Nature, 434, 159
Raftery, A. E. 1995, Sociological Methodology, 25, 111
Stephens, D. C., et al. 2009, ApJ, 702, 154
Su, L.-H., et al. 2021, AJ, 161, 108
Tabata, H., & Itoh, Y. 2020, Int. J. Astron. Astrophys., 10, 89
Villanueva, G. L., Smith, M. D., Protopapa, S., Faggi, S., & Mandell, A. M. 2018, J. Quant. Spectrosc. Radiat. Transfer, 217, 86
von Essen, C., Cellone, S., Mallonn, M., Albrecht, S., Miculán, R., Müller, H. M., & Schmitt, J. H. M. M. 2017, A&A, 603, A20
Winn, J. N., Holman, M. J., Shporer, A., Torres, G., Mazeh, T., Latham, D. W., Frazier, S. J., & Stanek, K. Z. 2007, AJ, 134, 1707
Winn, J. N., Holman, M. J., Shporer, A., Torres, G., Mazeh, T., Latham, D. W., Frazier, S. J., & Stanek, K. Z. 2008, ApJ, 683, 1076
Woitke, P., & Helling, C. 2003, A&A, 399, 297
Yelle, R. V. 2004, Icarus, 170, 167

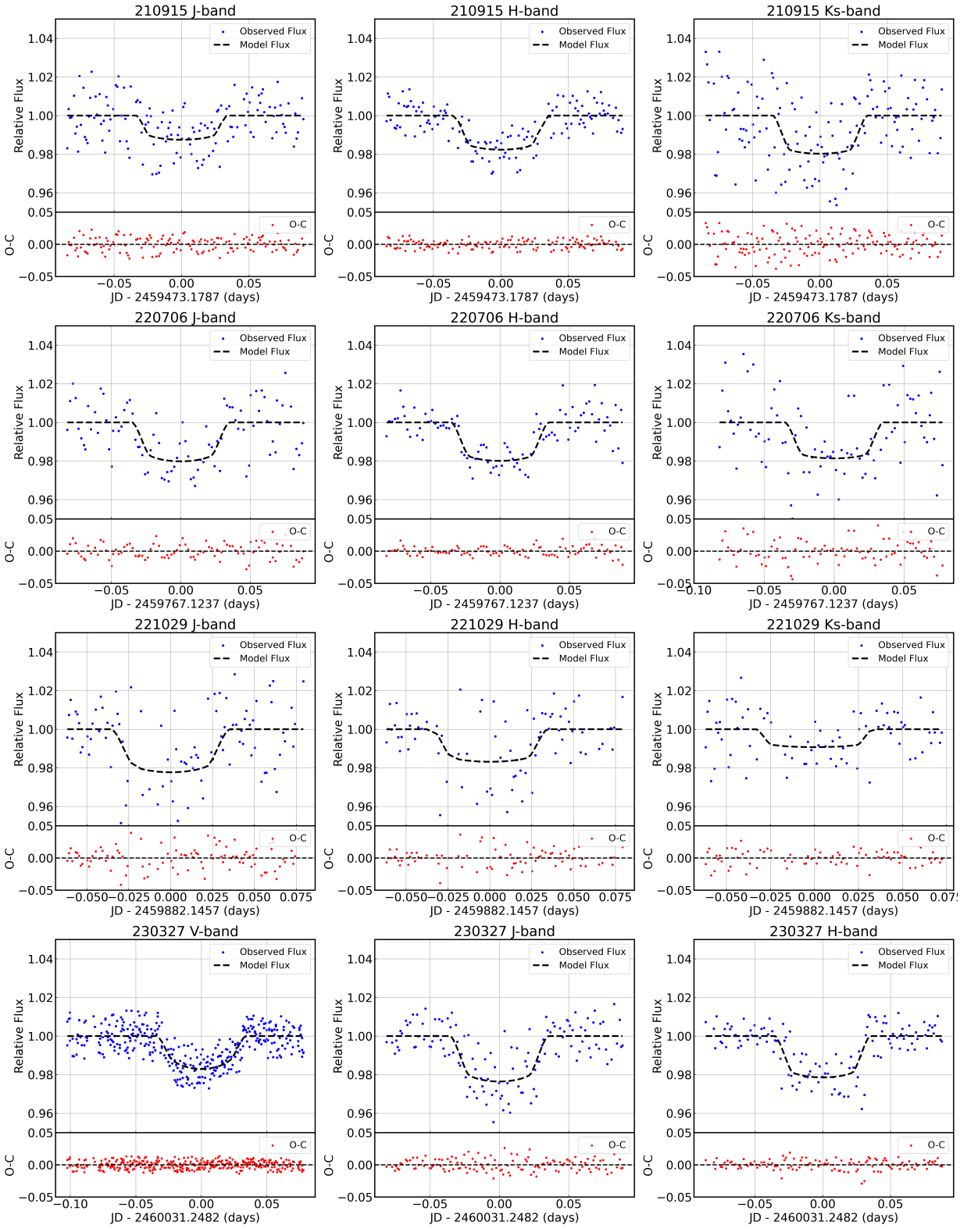

Fig. 6. The transit light curves of Qatar-1b observed from 2021 September 15 to 2023 October 12 are shown for multiple bands (V, J, H, and Ks). Each panel displays the relative flux as a function of time (top) and the residuals (O-C) between the observed and modeled fluxes (bottom). The blue points represent the observed relative flux, while the black dashed lines indicate the model flux. Observations are organized by date and band, starting with the V-band for each date. This figure includes data from the J-band observation on 2021 September 15 to the H-band observation on 2023 March 27.

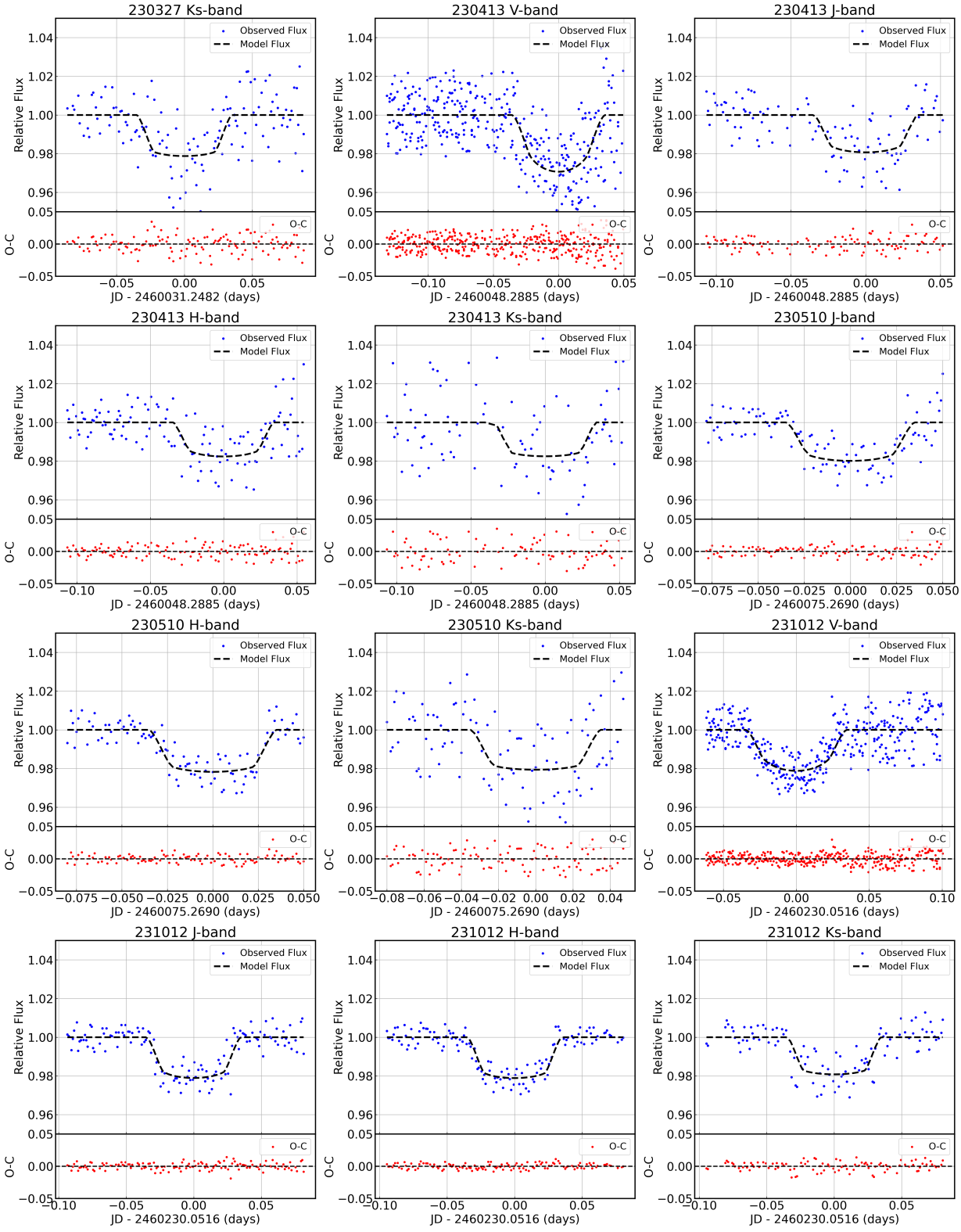

Fig. 7. The transit light curves of Qatar-1b observed from 2021 September 15 to 2023 October 12 are shown for multiple bands (V, J, H, and Ks). Each panel displays the relative flux as a function of time (top) and the residuals (O-C) between the observed and modeled fluxes (bottom). The blue points represent the observed relative flux, while the black dashed lines indicate the model flux. Observations are organized by date and band, starting with the V-band for each date. This figure includes data from the Ks-band observation on 2023 March 27 to the Ks-band observation on 2023 October 12. Transit light curves of Qatar-1 b observed from 2021 to 2023 for V, J, H, and Ks bands. Panels show relative flux over time (top) and residuals (O-C) between observed and modeled fluxes (bottom). Blue points indicate observed flux, and black dashed lines represent model flux.

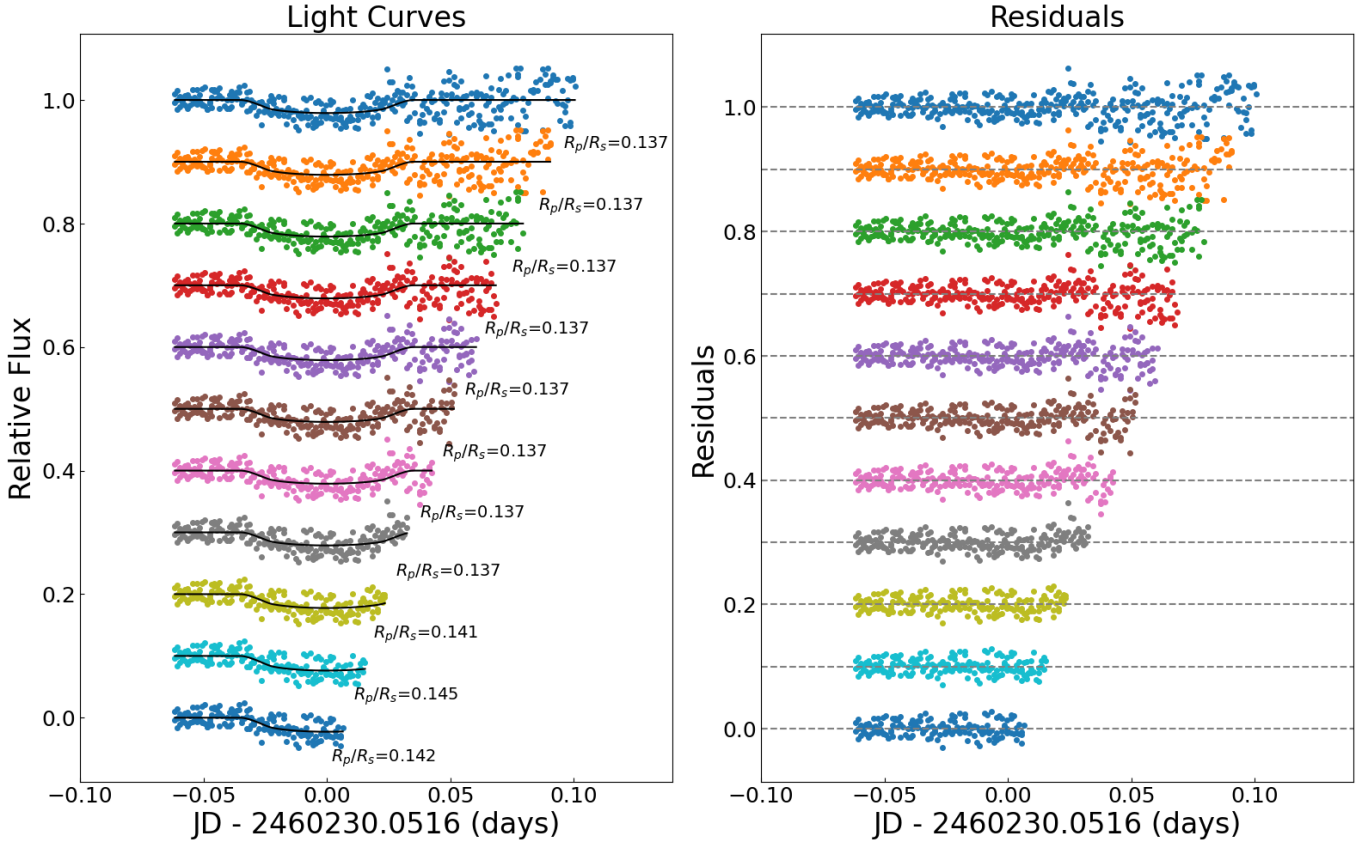

Fig. 8. The left panel shows the light curves of the 2023 October 12 V-band observation, which were used to evaluate the baseline conditions of the 2023 April 13 V-band observation. To simulate the observing conditions of 2023 April 13, the residuals of the 2023 October 12 dataset were multiplied by a constant factor to artificially degrade the data quality. Additionally, the post-transit baseline was systematically shortened in increments of 10 minutes, starting from the end of the observation. Each row corresponds to a dataset with progressively shorter post-transit baselines. The points represent the observed relative flux, while the solid lines indicate the best-fit models. The radius ratio remained stable at 0.137, even when the post-transit baseline was entirely removed (4th light curve from the bottom). The right panel shows the residuals between the observed data and the best-fit models for each light curve in the left panel.